Electronic Supplementary Material

The Magnetic Properties of $MAl_4(OH)_{12}SO_4 \cdot 3H_2O$ with M = Co^{2+}, Ni^{2+}, and Cu^{2+} Determined by a Combined Experimental and Computational Approach

Anders B. A. Andersen[1], Rasmus Tang Christiansen[2,3], Sofie Holm-Janas[2,4], Anna S. Manvell[5], Kasper S. Pedersen[5], Denis Sheptyakov[6], Jan Peter Embs[6], Henrik Jacobsen[6], Edgar Dachs[7], Juha Vaara[8], Kim Lefmann[2], Ulla Gro Nielsen[1,*]

[1]Department of Physics, Chemistry and Pharmacy, University of Southern Denmark, Campusvej 55, DK-5230 Odense, Denmark

[2]Nanoscience Center, Niels Bohr Institute, University of Copenhagen, Universitetsparken 5, DK-2100 Copenhagen Ø, Denmark

[3]Institut Laue Langevin, 71 Avenue des Martyrs, F-38042 Grenoble Cedex 9, France

[4] Current address: Department of Physics, Technical University of Denmark, DK-2800 Kongens Lyngby, Denmark

[5]Department of Chemistry, Technical University of Denmark, DK-2800 Kongens Lyngby, Denmark

[6]Laboratory for Neutron Scattering and Imaging, Paul Scherrer Institut, CH-5232 Villigen PSI, Switzerland

[7]Department of Chemistry and Physics of Materials, Universität Salzburg, Jakob-Haringerstrasse 2a, A-5020 Salzburg, Austria

[8]NMR Research Unit, University of Oulu, FI-90014 Oulu, Finland

*Corresponding author: ugn@sdu.dk +45 6550 4401

Contents

S1: Additional Information on Bulk Magnetic Measurements

Magnetization Equations

The equations derived from perturbation theory (SI units) for the parallel ($M_{||}$) and perpendicular ($M_{\perp}$) magnetization as a function of field (B) and temperature (T) for an axial ($E = 0$) ZFS system are given below for $S = 1$ (S1-3). The reader is referred to Ref.[1] for additional information.

For S = 1:

$$M_{||} = \frac{N_A \mu_B g}{Z_{||}} \left[\exp\left\{ -\frac{D-G}{k_B T} \right\} - \exp\left\{ \frac{D+G}{k_B T} \right\} \right], \tag{S1}$$

$$M_{\perp} = \frac{N_a \mu_B g G}{Z_{\perp} \sqrt{D^2/4+G^2}} \left[\exp\left\{ -\frac{D/2-\sqrt{D^2/4+G^2}}{k_B T} \right\} - \exp\left\{ -\frac{D/2+\sqrt{D^2/4+G^2}}{k_B T} \right\} \right] \tag{S2}$$

$$Z_{||} = 1 + \exp\left\{ -\frac{D+G}{k_B T} \right\} + \exp\left\{ -\frac{D-G}{k_B T} \right\} \tag{S3}$$

where $C_0 = N_A \mu_0 \mu_B^2 / k_B$, $\delta = D/(k_B T)$, $d = e^{-\delta}$, D is the ZFS parameter, g is the electron g-factor, N_A is Avogadro's number, μ_0 is the vacuum permeability, μ_B is the Bohr magneton, k_B is Boltzmann's constant. $G = g \mu_B B$ and the applied field is assumed to be equal in all directions, as appropriate for a powder sample in a uniform field. The powder-averaged magnetization is calculated as $M_{avg} = (2M_{\perp} + M_{||})/3$.

Heat Capacity

To estimate the non-magnetic contributions to the heat capacity (C_p), diamagnetic $ZnAl_4$-LDH was used as a reference material.[2, 3] Unfortunately, the phonon contribution to the C_p of $ZnAl_4$-LDH was not equal to those of the magnetic samples despite their isomorphism, as a subtraction of the $ZnAl_4$-LDH C_p yielded negative $C_{p,mag}/T$-values for all the magnetic compounds (Fig. S5b). A similar situation was previously encountered for, *e.g.*, the magnetic compound $GdCoIn_5$ and its non-magnetic isomorph $LaCoIn_5$.[4] Inclusions of the small difference in the molar weight and unit cell volumes of the four LDHs, by scaling the temperature for the $ZnAl_4$-LDH C_p/T-data by a Lindeman factor,[5] did

not resolve this issue. Furthermore, an estimate of the phonon contribution on the basis of the Debye and Einstein terms[6] was not feasible due to the complexity of the unit cell. Thus, quantitative assessment of the magnetic properties of the LDHs on the basis of $C_{p,mag}$ proved unsuccessful.

Despite these challenges, a qualitative inspection of the data still gives valuable information. First, we observe, that C_p only shows broad features at low temperatures, and no signs of transition to a long-range magnetic order in the form of λ-shaped anomalies are found. Second, significant positive values of the subtracted C_p/T at low temperatures ($T < 30$ K) are found, which confirm the existence of a magnetic contribution to C_p, as expected from our magnetization and inelastic neutron scattering measurements.

S2: Additional Information on Neutron Scattering

Neutron Diffraction

The $\chi(T)$ data for $DNiAl_4$-LDH revealed no transition to long-range magnetic order for $T > 2$ K. To confirm the absence of long-range magnetic order, neutron diffraction was performed at $T = 1.6$ K (Fig. S6a) and $T = 50$ K (Fig. S6b) at the instrument HRPT at SINQ, PSI, Switzerland.[7] A magnetic signal would manifest itself as a difference between the high-T and low-T data. However, the two diffractograms appear identical and no signs of even a precursor to ferromagnetic ordering, such as a weak, broad signal at a position of the reciprocal lattice vector, are observed. Even the difference, $\Delta I = I_{1.6\,K} - I_{50\,K}$, contains no features (Fig. S6c), confirming the absence of any magnetic signals.

Neutron Spectroscopy

The full neutron spectrum of $D\text{-}NiAl_4$-LDH at 2 K and 100 K recorded at FOCUS, PSI[8] is presented in Fig. S1. A dispersionless excitation at $\Delta E \approx 0.8$ meV is observed at both temperatures, representing the ZFS. Moreover, a complementary excitation at $\Delta E \approx -0.8$ meV is observed only at $T = 100$ K, in

agreement with the principle of detailed balance.[9] The integrated intensity of the excitation falls off with increasing $|Q|$ (Fig. S2), as expected for a magnetic signal due to the magnetic form factor.[9] The neutron spectroscopy data for D-$NiAl_4$-LDH were corrected for the background by subtraction of the empty sample holder signal. Since the excitation is flat, the data was integrated over the entire $|Q|$-range to obtain an $I(E)$ curve. It was modelled as a sum of delta functions to account for elastic, incoherent scattering, a Lorentzian to model the quasi-elastic signal, and two Gaussians, which reflect the ZFS excitation at positive and negative energy transfers, respectively. The model is given by $\mathrm{Inc}(E) + Q(E) + \mathrm{CF}(E)$, where $\mathrm{Inc}(E) = A_1\delta(E)$ with A_1 being the amplitude of the incoherent signal; $Q(E) = A_q\Gamma / (2\pi (E^2+(\Gamma/2)^2))$ is the Lorentzian with an area of A_q and the full width half max (FWHM) Γ of the quasielastic scattering. The crystal-field signal is given by $\mathrm{CF}(E) = A_{cf1}\,\mathrm{Gauss}(E_{cf}, \sigma) + A_{cf2}\mathrm{Gauss}(-E_{cf}, \sigma)$, where E_{cf} is the crystal-field splitting, A_{cf1} and A_{cf2} the area of the signals and $\mathrm{Gauss}(E, \sigma)$ represents a Gaussian line profile centred at E and with a standard deviation of σ. This model is then convoluted with the instrumental resolution to obtain the final model. The resolution was determined by fitting a Gaussian line profile to the central, incoherent part of the elastic line in the $|Q|$-integrated data (Fig. 3a). This yielded $A = 53.11(2)$ meV, $\mu = 0.070(14)$ meV, and $\sigma = 41.7(9)$ μeV. The DAVE software[9] was used to reduce the raw time-of-flight data, and Mslice[8] was used for data cutting and integration. The fitting was performed with the Mantid fitting tool.[10] For a direct-geometry time-of-flight spectrometer, the resolution narrows as the energy transfer value increases at the energy loss side (positive values of E). Since the crystal-field signals needed to be modelled by a Lorentzian before being convoluted with the resolution, the excitation must have an intrinsic broadening, which is ascribed to molecular strain.

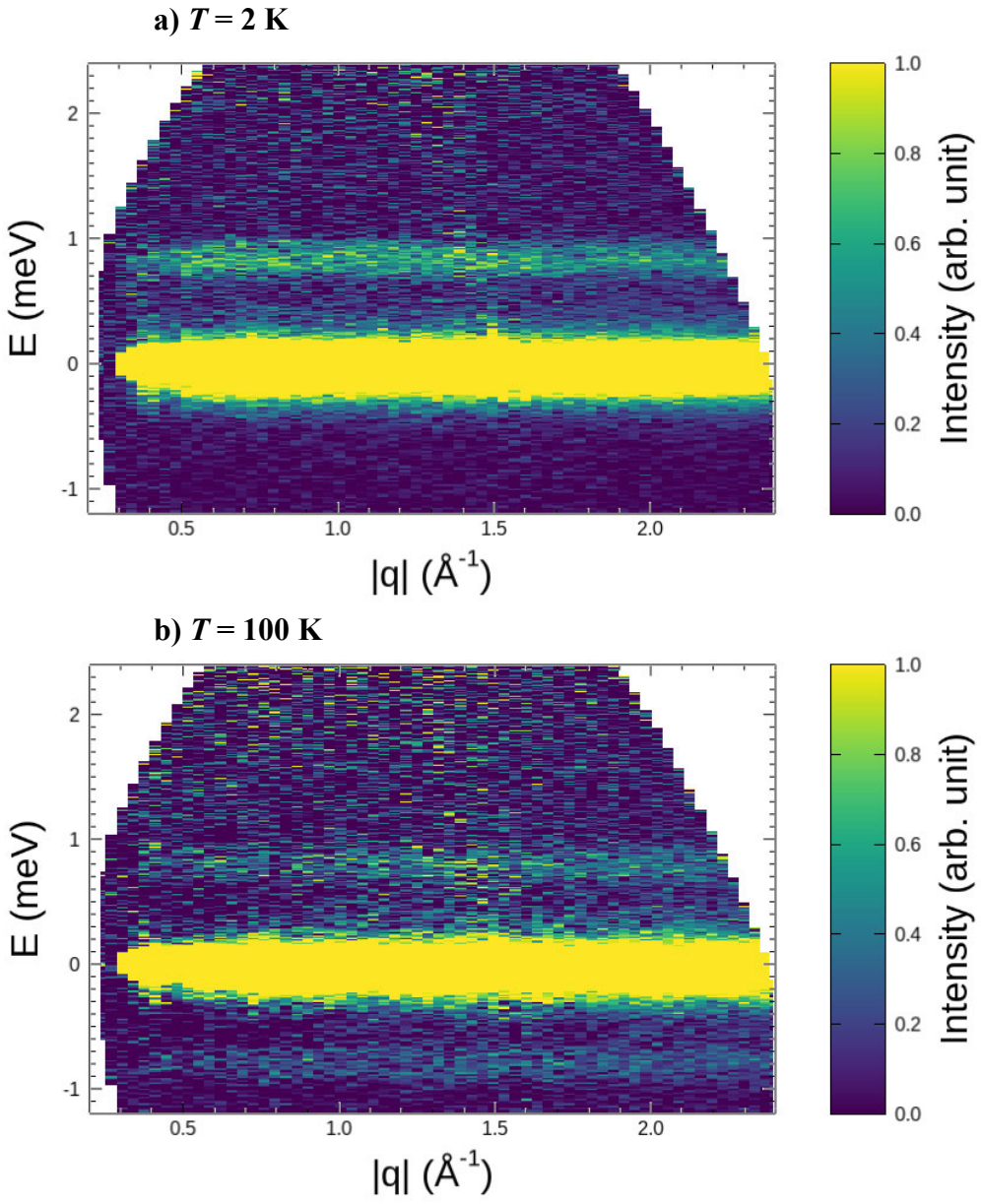

Fig. S1: Inelastic neutron scattering intensity vs. energy transfer and modulus of the scattering vector of D-NiAl$_4$-LDH at **a)** $T = 2$ K and **b)** $T = 100$ K measured at FOCUS[8] (PSI) with $E_i = 3.55$ meV corrected for background signal. The diffuse features running from $|q| = 1.5$ Å^{-1} at the elastic line to $|q| = 1.2$ Å^{-1} at $E = 2$ meV are artefacts caused by the detector.

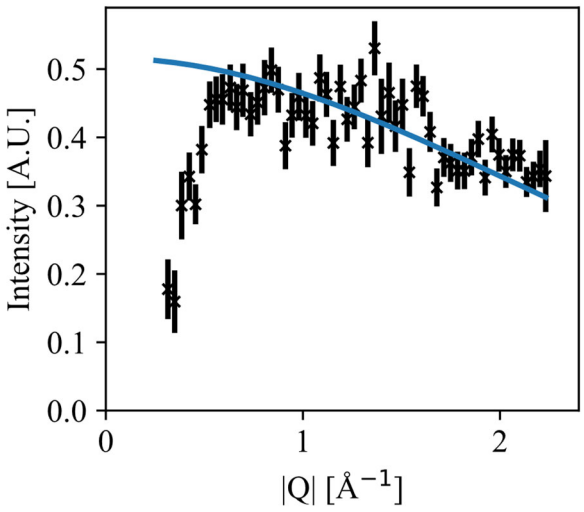

Fig. S2: $|Q|$-dependence of the integrated intensity I_{int} of the ZFS excitation at $\Delta E = 0.8358(17)$ meV, measured by inelastic neutron scattering on the D-NiAl$_4$-LDH sample at T = 1.6 K. The data is integrated from 0.65 meV to 1 meV. The blue line is the magnetic form factor of Ni^{2+} scaled to arbitrary units.[11] The decrease at low $|Q|$ is an artifact of being close to the border of the measured spectrum.

S3: Additional Information on the Computational Models

ORCA Formalism

In the broken-symmetry formalism of quantum-chemical calculations of the exchange coupling constant, two separate self-consistent field (SCF) calculations are performed: one for the high-spin state $S = \frac{N_A+N_B}{2}$ and one for the broken-symmetry state $S = \frac{N_A-N_B}{2}$, where N_A unpaired electrons are located on the coupled site A and N_B are located on site B. The two calculations give the respective energies, E_{HS} and E_{BS}, respectively. In the flip-spin formalism, the individual spin densities are also used in two separate SCF calculations. First the high-spin state is calculated, after which the low-spin state is optimized after exchanging the α and β spin blocks of the spin density on the coupled centers.[12] Then, J_{AB} can be extracted from the obtained E_{HS} and E_{BS}, the formal spins S_A and S_B, as well as the expectation values of the S^2 operator in the two SCF calculations, by three different formulae:[13-17]

$$J_{AB} = -\frac{E_{HS} - E_{BS}}{(S_A + S_B)^2} \tag{S4}$$

$$J_{AB} = -\frac{E_{HS} - E_{BS}}{(S_A + S_B)(S_A + S_B + 1)} \tag{S5}$$

$$J_{AB} = -\frac{E_{HS} - E_{BS}}{\langle S^2 \rangle_{HS} - \langle S^2 \rangle_{BS}}. \tag{S6}$$

Eq. (S4) is best adapted to the weak-coupling limit, Eq. (S5) to the strong-coupling limit, and Eq. (S6) remains approximately valid in the whole coupling strength regime. To ensure as high a numerical precision of the critically important energy differences as possible, the VeryTightSCF or TightSCF convergence criteria, with level 7 integration grids, were employed in ORCA.

Cluster Model Construction

Prior to geometry optimization, large models were constructed from the reported X-ray structure for the nickelalumite system by Uvarova *et al.*[18] using VESTA (ver. 3.4.8)[19] and Schrödinger Maestro (ver. 12.4), where the two adjacent magnetic Ni^{2+} centres were replaced by Co^{2+} or Cu^{2+} for $CoAl_4$- and $CuAl_4$-LDH, respectively. The clusters were terminated by pseudohydrogens,[20] H*, which in practice are point charges representing the missing bonds to either Al^{3+} or M^{2+}, with values set to +1/2 and +1/3 for Al^{3+} and M^{2+}, respectively, to render the formal valence of all the explicit cluster atoms correct. The bond distances of terminating pseudohydrogens and the terminal oxygens were set to 1.10 Å. Geometry optimization was first carried out on the large cluster models in TURBOMOLE[21] (ver. 7.5) with fixed atomic positions of the pseudohydrogens. First, the resolution of the identity density-functional theory (RIDFT) was used with the standard gradient-corrected, pure PBE functional,[22, 23] *i.e.*, with 0% exact Hartree–Fock exchange. Subsequently, the hybrid PBE0 functional,[24] *i.e.,* with 25% exact exchange, as well as the DFT-D3 BJ dispersion correction, were employed.[25, 26] These methods were employed with the Stuttgart-type scalar-relativistic effective core potentials ECP10MDF,[27] along with the corresponding valence basis sets on the M^{2+} and Zn^{2+} ions, def2-SV(P) basis set[28] on the pseudohydrogens, and def2-TZVP[28] on the Al, O, and H atoms. The geometry-optimized medium- and small-size cluster models were constructed from the optimized, large cluster models, by cutting the appropriate atoms and adding the termination pseudohydrogens as above. We note that the crystal symmetry was not retained leading to a single *J* value, as experimentally only a single *J* is obtained. In the crystal structure, *J* can be mediated via Al1 or Al2, which structurally are very similar. the large inter-chain models were only geometry optimized at the PBE level, due to the demanding nature of the hybrid PBE0 computations. The optimized coordinates are given as .xyz files and are available for download as a .zip folder as electronic supporting information.*Single-Site Property Calculations*

The magnetic parameters ***g*** and ***D*** were obtained by a quasidegenerate perturbation theory process that involves diagonalization of the mean-field spin-orbit interaction in the basis of the one-component state-average CASSCF wave functions.[29, 30] The calculations involved multireference perturbation theory in the form of strongly contracted NEVPT2, in which, for M = Cu^{2+}, 5 doublet states, for M = Ni^{2+}, 10 triplet and 15 singlet states, and for M = Co^{2+},10 quartet and 40 doublet states were included. In the case of the medium-size models, the more efficient domain-based local pair natural orbital NEVPT2 (DLPNO-NEVPT2) method[31] was employed. Note that the large single-M^{2+} cluster models were omitted from the calculations of ***g*** and ***D***, as these calculations were extremely demanding, and the CASSCF-level results changed relatively little between the small and medium-size single-site cluster models (see Fig. S3).

Table S1: Information for the cluster models used for the in-chain exchange coupling, *J*, calculations (Fig. 1c). Total number of atoms including cluster-terminating pseudohydrogens (n_{atoms}), number of pseudohydrogens with a charge of +1/2 [n_{H^*} (1/2)], number of pseudohydrogens with a charge of +1/3 [n_{H^*} (1/3)], total charge of pseudohydrogens (Tot. H^* charge), total charge of the entire cluster (Tot. charge), and total number of electrons in the cluster (n_{e^-} (Co), n_{e^-} (Ni), and n_{e^-} (Cu), for $CoAl_4$-, $NiAl_4$- and $CuAl_4$-LDH, respectively).

Size	n_{atoms}	n_{H^*} **(1/2)**	n_{H^*} **(1/3)**	**Tot.** H^* **charge**	**Tot. charge**	n_{e^-} **(Co)**	n_{e^-} **(Ni)**	n_{e^-} **(Cu)**
Small	110	16	6	10	6	530	532	534
Medium	220	32	12	20	12	1066	1068	1070
Large	338	44	18	28	22	1718	1720	1722

Table S2: Information for the cluster models used for the inter-chain exchange coupling, *j*, calculations (Fig. 1d). Total number of atoms including pseudohydrogens (n_{atoms}), the number of pseudohydrogens with a charge of +1/2 [n_{H^*} (1/2)], the number of pseudohydrogens with a charge of +1/3 [n_{H^*} (1/3)], the total charge of the pseudohydrogens (Tot. H^* charge), the total charge of the entire cluster (Tot. charge), and the total number of electrons in the cluster (n_e- (Co), n_e- (Ni), and n_e- (Cu), for $CoAl_4$-, $NiAl_4$- and $CuAl_4$-LDH, respectively).

Size	n_{atoms}	n_{H^*} **(1/2)**	n_{H^*} **(1/3)**	**Tot.** H^* **charge**	**Tot. charge**	n_e- **(Co)**	n_e- **(Ni)**	n_e- **(Cu)**
Small	138	20	12	14	8	630	632	634
Medium	274	56	0	28	16	1378	1380	1382
Large[a]	378	40	24	28	24	1938	1940	1942

[a]The large cluster was only used for the geometry optimizations

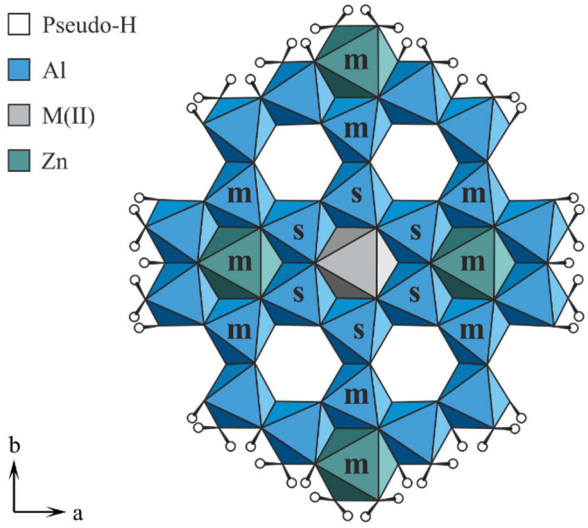

Fig. S3: Single-site magnetic cluster models used for the calculations of the single-site properties. The entire cluster was used for the large model, whereas *m* and *s* signify the extent of the medium and small models, respectively.

Table S3: Information for single magnetic-M cluster models used for the single-site property, ***D*** and ***g***, calculations (Fig. S3). The total number of atoms including pseudohydrogens (n_{atoms}), the number of pseudohydrogens with a charge of +1/2 [n_{H^*} (1/2)], the number of pseudohydrogens with a charge of +1/3 [n_{H^*} (1/3)], the total charge of all pseudohydrogens (Tot. H^* charge), the total charge of the entire cluster (Tot. charge), and total number of electrons in the cluster (n_{e^-} (Co), n_{e^-} (Ni), and n_{e^-} (Cu), for $CoAl_4$-, $NiAl_4$- and $CuAl_4$-LDH, respectively).

Size	n_{atoms}	n_{H^*} **(1/2)**	n_{H^*} **(1/3)**	**Tot.** H^* **charge**	**Tot. charge**	n_{e^-} **(Co)**	n_{e^-} **(Ni)**	n_{e^-} **(Cu)**
Small	73	12	6	8	4	325	326	327
Medium	177	44	0	22	10	837	838	839
Large[a]	255	32	18	22	16	1257	1258	1259

[a]The large clusters were only used for the geometry optimizations, not for the calculations of ***g*** and ***D***.

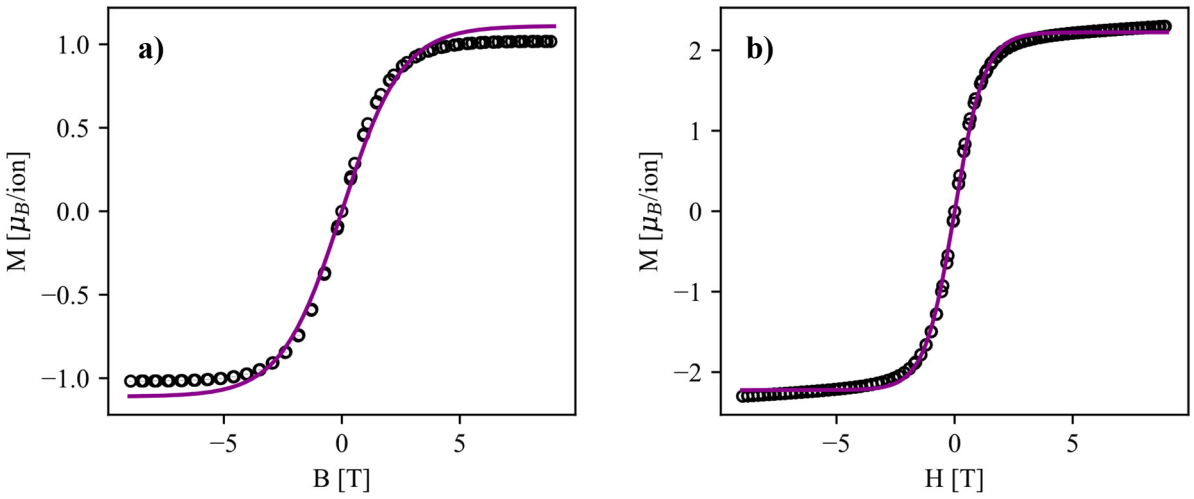

Fig. S4: Supplemental bulk magnetization measurements of MAl_4-LDH. **a)** $M(B)$ (black) for $CuAl_4$-LDH measured at $T = 1.9$ K with a fitted Brillouin function (purple $S = 1/2$). The Brillouin fit for the Cu system clearly does not reproduce the measurements. **b)** $M(B)$ of $CoAl_4$-LDH measured at $T = 1.9$ K (black) fitted with a fictious S' = 1/2 Brillouin (purple) yielding $g_{eff} = 4.45(5)$, *i.e.*, close to the expected $g_{eff} = 4.3$ for a Co^{2+} ion in O_h symmetry.

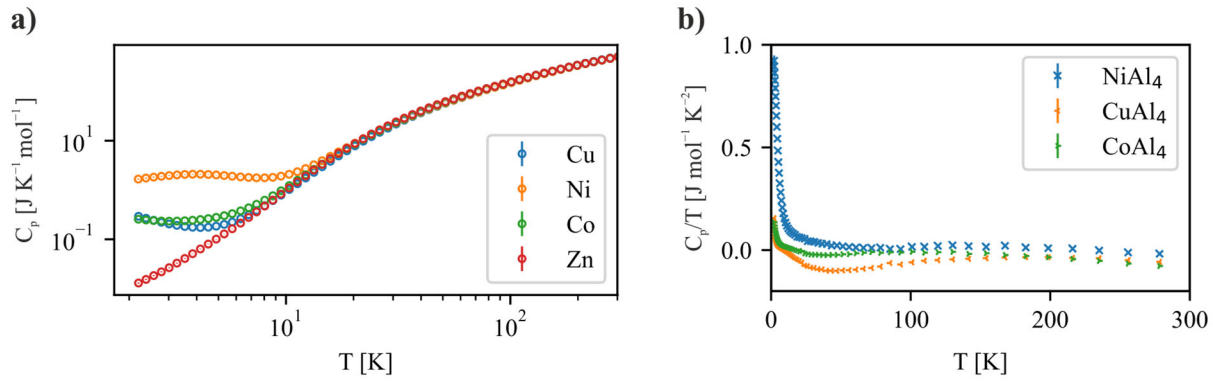

Fig. S5: a) Total heat capacity for the MAl_4-LDH samples with M = Cu^{2+}, Ni^{2+}, Co^{2+} and Zn^{2+} plotted on a double-logarithmic scale. **b)** Attempt at extracting the magnetic C_p/T parameter for $CuAl_4$-, $NiAl_4$-, and $CoAl_4$-LDH by subtraction of the $ZnAl_4$-LDH data scaled by a Lindeman factor.[5] The negative C_p/T-values especially observed for $CuAl_4$-LDH imply that phonon contribution was not accurately accounted for by this method.

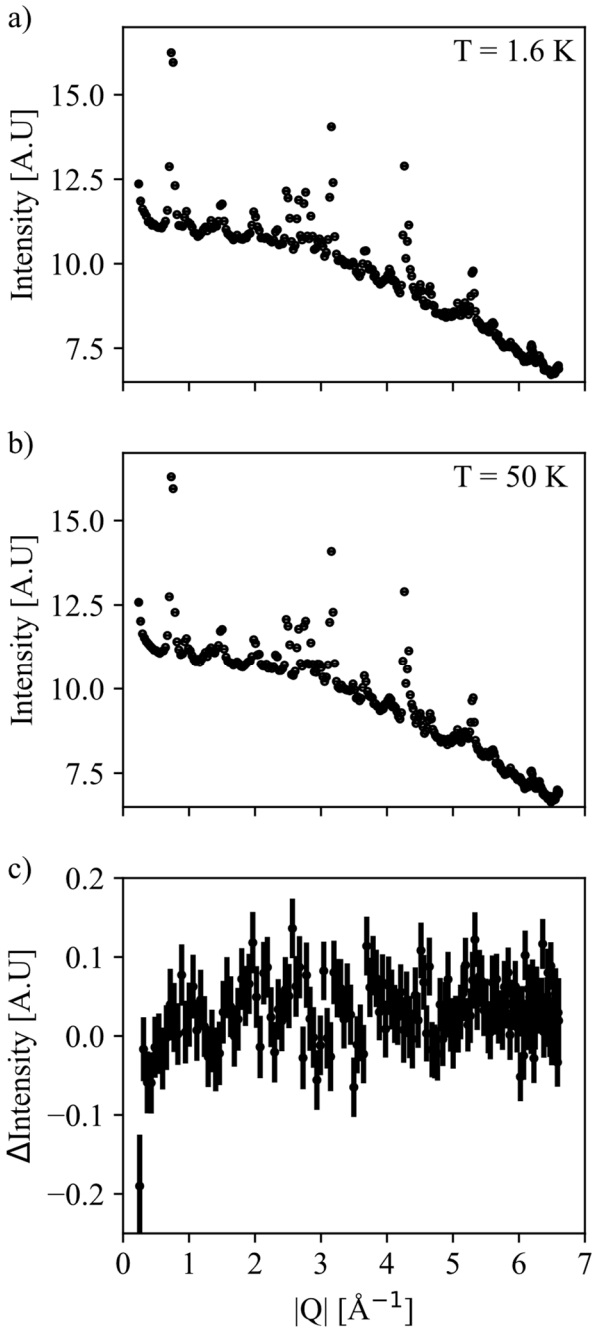

Fig. S6: Neutron diffractograms of DNiAl4-LDH measured with λ_i = 1.886 Å at **a)** T = 1.6 K and **b)** T = 50 K at HRPT, PSI.[7] **c**) The intensity difference, $\Delta I = I_{1.6\,K} - I_{50\,K}$ between the two diffractograms. It contains no sharp features with $\Delta I > 0$ and thus the absence of long-range magnetic order is confirmed.

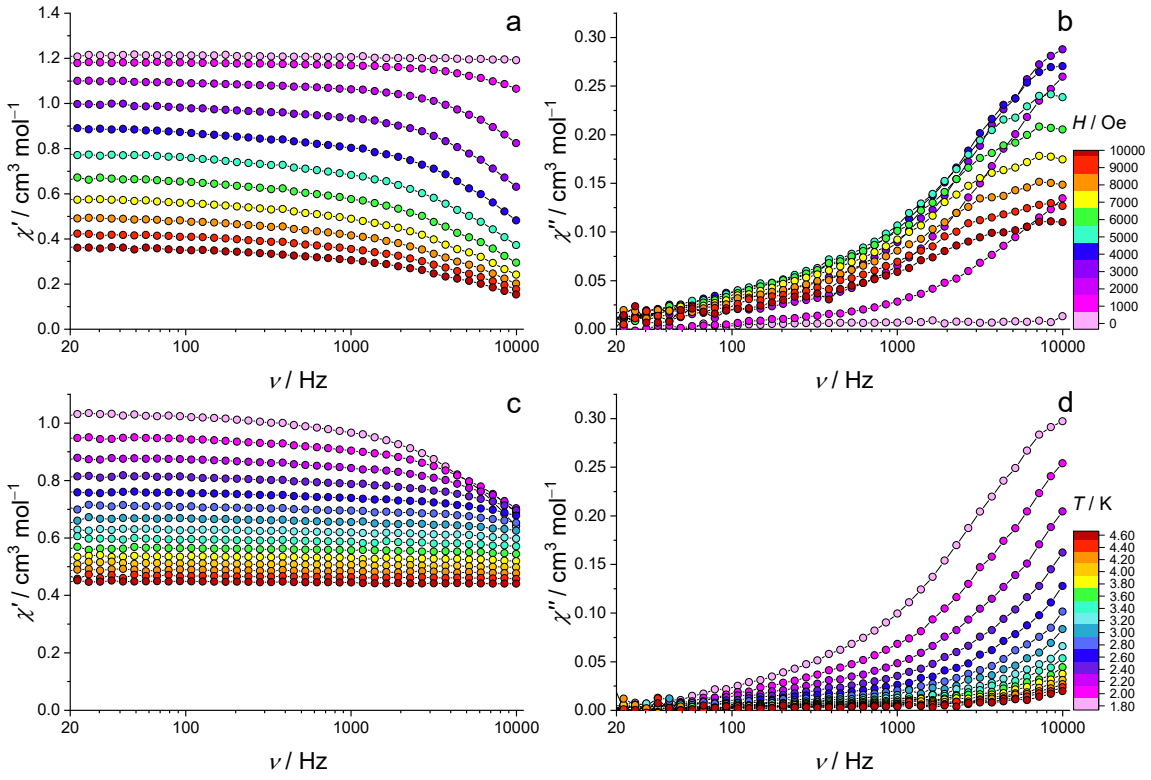

Fig. S7. a) Real and b) imaginary part of the AC susceptibility of $CoAl_4$-LDH as a function frequencyf or the different applied dc magnetic field at T = 1.8 K.)**.** c) Real and d) imaginary part of the AC susceptibilty at various temperaturs at $\mu_0 H_{dc}$ fixed to 3000 Oe.

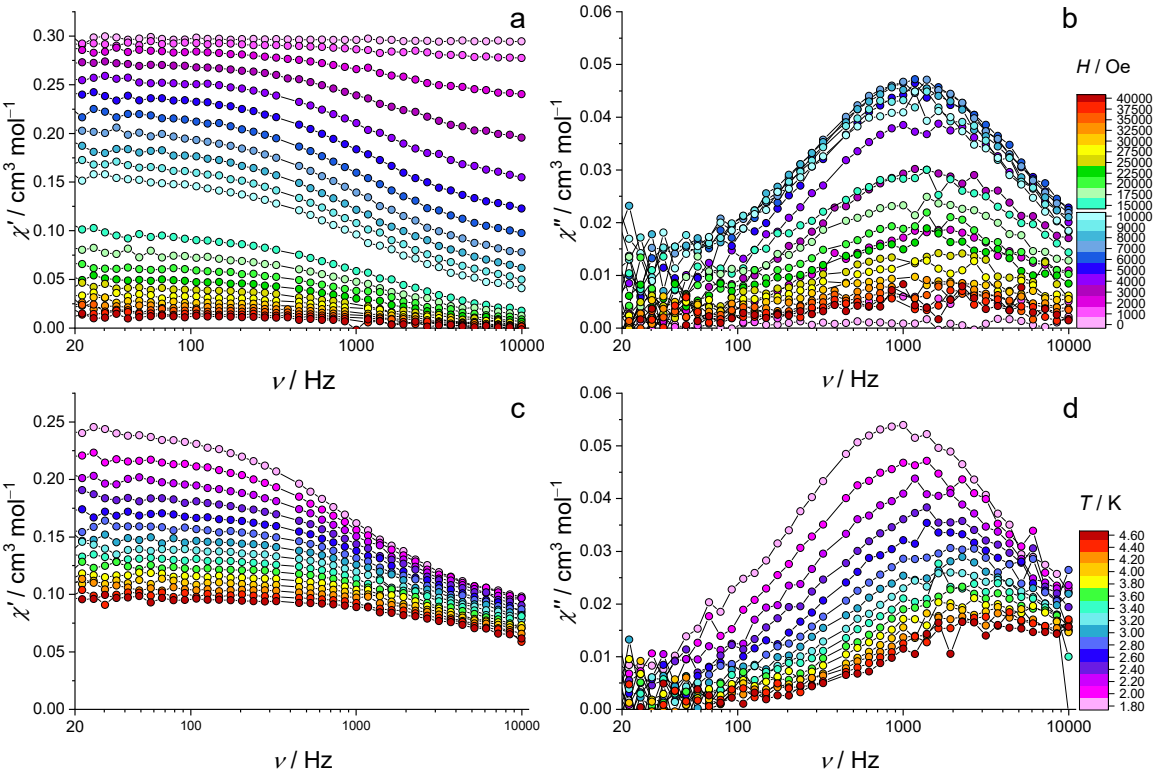

Fig. S8. a) Real and b) imaginary part of the AC susceptibility of $CuAl_4$-LDH as a function of the applied dc magnetic field at T = 1.8 K. c) Real and d) imaginary part of the AC susceptibility as a function of temperature at $\mu_0 H_{dc}$ fixed at 6000 Oe

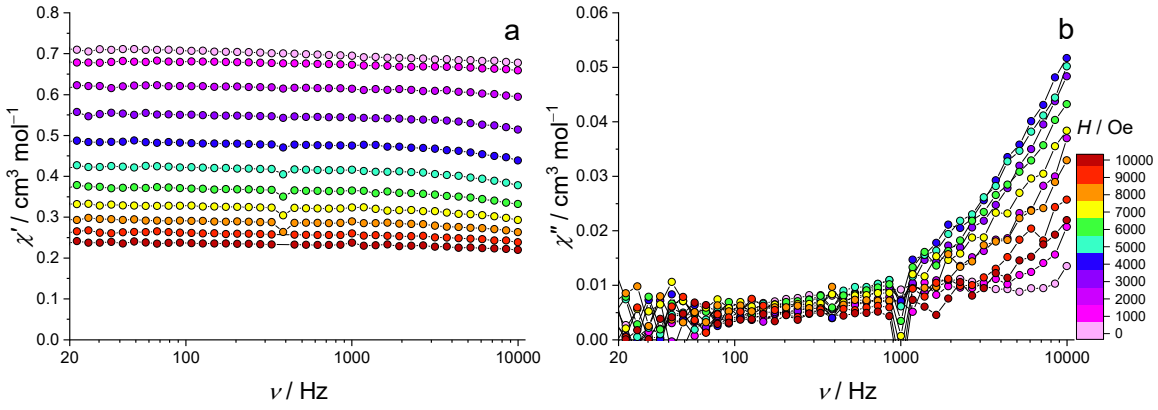

Fig. S9. a) Real and b) imaginary part of the AC susceptibility of $NiAl_4$-LDH as a function of the applied dc magnetic field at T = 1.8 K.

Table S4: Computational results for in-chain exchange coupling, *J*, from calculations of the small, medium, and large-size in-chain cluster models (Fig. 1c). The results are reported in the broken-symmetry formalism and flip-spin formalism in parentheses. *J*(1), *J*(2), and *J*(3) correspond to the weak (Eq. S4), strong (Eq. S5) and general (Eq. S6) coupling regimes, see page S9.

Functional	**Basis set**	**Formula**	**Cu**			**Ni**			**Co**		
Geometry			**Small**	**Medium**	**Large**	**Small**	**Medium**	**Large**	**Small**	**Medium**	**Large**
PBE0	SVP	*J*(1)	0.67	1.04	0.35	0.17	0.11	0.08	0.02	0.06	0.04
Functional			(0.66)	(0.89)	(0.07)	(0.15)	(0.04)	(0.16)	(-0.04)	(0.08)	(-0.22)
		J(2)	0.34	0.52	0.18	0.11	0.08	0.05	0.02	0.05	0.03
@PBE-			(0.33)	(0.45)	(0.04)	(0.10)	(0.03)	(0.11)	(-0.03)	(0.06)	(-0.17)
optimized		*J*(3)	0.67	1.04	0.35	0.17	0.11	0.08	0.02	0.06	0.04
geometry			(0.66)	(0.89)	(0.07)	(0.15)	(0.04)	(0.16)	(-0.04)	(0.08)	(-0.22)
	QZVPP/SVP	*J*(1)	0.71	0.87	0.21	0.19	0.15	0.11	0.09	0.06	0.04
			(0.69)	(0.60)	(0.98)	(0.18)	(0.18)	(0.16)	(0.08)	(--[a])	(0.06)
		J(2)	0.35	0.43	0.11	0.13	0.1	0.07	0.07	0.05	0.03
			(0.34)	(0.30)	(0.49)	(0.12)	(0.12)	(0.11)	(0.06)	(--[a])	(0.04)
		J(3)	0.71	0.87	0.21	0.19	0.15	0.11	0.09	0.06	0.04
			(0.69)	(0.60)	(0.98)	(0.18)	(0.18)	(0.16)	(0.08)	(--[a])	(0.06)
PBE0	SVP	*J*(1)	0.58	0.80	0.49	0.14	0.07	0.09	0.04	0.06	0.06
Functional			(0.58)	(0.65)	(0.69)	(0.15)	(0.05)	(0.03)	(0.04)	(0.03)	(0.07)
		J(2)	0.29	0.40	0.25	0.090	0.04	0.06	0.03	0.05	0.05
@PBE0-			(0.29)	(0.32)	(0.34)	(0.10)	(0.03)	(0.02)	(0.03)	(0.02)	(0.05)
optimized		*J*(3)	0.58	0.80	0.49	0.14	0.07	0.09	0.04	0.06	0.06
geometry			(0.58)	(0.65)	(0.69)	(0.15)	(0.05)	(0.03)	(0.04)	(0.03)	(0.07)
	QZVPP/SVP	*J*(1)	0.63	0.50	0.65	0.20	0.15	0.27	0.06	0.06	--[a]
			(0.67)	(0.60)	(0.72)	(0.20)	(0.18)	(0.17)	(0.09)	(0.12)	(0.10)
		J(2)	0.32	0.25	0.32	0.13	0.1	0.18	0.05	0.05	--[a]
			(0.33)	(0.30)	(0.36)	(0.13)	(0.12)	(0.11)	(0.06)	(0.09)	(0.08)
		J(3)	0.63	0.50	0.65	0.20	0.15	0.27	0.06	0.06	--[a]
			(0.67)	(0.60)	(0.72)	(0.20)	(0.18)	(0.17)	(0.09)	(0.12)	(0.10)
PBE0-40	SVP	*J*(1)	0.38	0.22	0.20	0.11	0.04	0.13	0.03	0.02	0.03
functional			(0.29)	(0.45)	(0.57)	(0.11)	(0.06)	(0.1)	(0.05)	(0.05)	(0.07)
		J(2)	0.19	0.11	0.10	0.07	0.03	0.09	0.02	0.02	0.02
@PBE0-			(0.15)	(0.23)	(0.29)	(0.07)	(0.04)	(0.07)	(0.04)	(0.04)	(0.05)
optimized		*J*(3)	0.38	0.22	0.20	0.11	0.04	0.13	0.03	0.02	0.03
geometry			(0.29)	(0.45)	(0.57)	(0.11)	(0.06)	(0.1)	(0.05)	(0.05)	(0.07)
	QZVPP/SVP	*J*(1)	0.29	0.25	0.55	0.15	0.06	0.14	0.01	0.06	--[a]
			(0.25)	(0.35)	(0.42)	(0.13)	(0.11)	(0.19)	(0.03)	(0.10)	(0.08)
		J(2)	0.14	0.12	0.28	0.10	0.04	0.09	0.01	0.05	--[a]
			(0.13)	(0.18)	(0.21)	(0.09)	(0.08)	(0.13)	(0.02)	(0.07)	(0.06)
		J(3)	0.29	0.25	0.55	0.15	0.06	0.14	0.01	0.06	--[a]
			(0.25)	(0.35)	(0.42)	(0.13)	(0.11)	(0.19)	(0.03)	(0.10)	(0.08)

[a] Reliable data could not be obtained.

Table S5: Results for exchange coupling, *j*, calculations of the small and medium-size inter-chain cluster models (Fig. 1d), using the PBE0 functional at the PBE-optimized geometry. The results are reported in the broken-symmetry formalism (flip-spin formalism in parentheses). The cluster geometries were optimized using the PBE functional. *j*(1), *j*(2), and *j*(3) correspond to the weak (Eq. S4), strong (Eq. S5) and general (Eq. S.6) coupling regimes, see page S9.

Basis set	**Formula**	**Cu**		**Ni**		**Co**	
		Small	**Medium**	**Small**	**Medium**	**Small**	**Medium**
SVP	*j*(1)	0.08	-0.05	0.00	-0.02	0.04	-0.05
		(-0.44)	(-0.17)	(-0.01)	(-0.07)	(0.00)	(--[a])
	j(2)	0.04	-0.03	0.00	-0.01	0.03	-0.04
		(-0.22)	(-0.08)	(-0.01)	(-0.04)	(0.00)	(--[a])
	j(3)	0.08	-0.05	0.00	-0.02	0.04	-0.05
		(-0.44)	(-0.17)	(-0.01)	(-0.07)	(0.00)	(--[a])
QZVPP/SVP	*j*(1)	-1.18	-0.03	-0.02	-0.06	0.00	--[a]
		(-2.83)	(-0.01)	(-0.02)	(-0.04)	(-0.18)	(0.00)
	j(2)	-0.59	-0.01	-0.01	-0.04	0.00	--[a]
		(-1.42)	(0.00)	(-0.01)	(-0.03)	(-0.13)	(0.00)
	j(3)	-1.18	-0.03	-0.02	-0.06	0.00	--[a]
		(-2.83)	(-0.01)	(-0.02)	(-0.04)	(-0.18)	(0.00)

Table S6: Results for the single site-property, ***g*** and ***D***, calculations of the single magnetic-center cluster models (Fig. S3). The results are reported for the PBE0-optimized cluster geometries (for PBE geometries in parentheses).

Method	**Property**	**Cu**[a]		**Ni**		**Co**	
		Small	**Medium**	**Small**	**Medium**	**Small**	**Medium**
CASSCF	*g*-factors	2.69	2.18	2.28(2.29)	2.28(2.29)	1.93(1.91)	1.93(1.91)
		2.12	2.00	2.29(2.30)	2.29(2.30)	2.67(2.63)	2.69(2.62)
		2.13	2.13	2.35(2.36)	2.35(2.36)	2.76(2.80)	2.74(2.82)
	g_{iso}	2.31	2.11	2.31(2.32)	2.31(2.32)	2.45(2.45)	2.46(2.45)
	D [cm^{-1}]	--	--	-10.5(-10.6)	-10.5(-10.6)	101.4(106.9)	100.9(106.4)
	E/*D*	--	--	0.025(0.038)	0.022(0.034)	0.037(0.062)	0.022(0.073)
NEVPT2	*g*-factors	2.52	2.13[b]	2.21(2.22)	2.22[ab]	1.87(1.84)	1.88[ab]
		2.10	2.01[b]	2.27(2.23)	2.22[ab]	2.64(2.36)	2.65[ab]
		2.11	2.10[b]	2.27(2.27)	2.27[ab]	2.78(2.81)	2.77[ab]
	g_{iso}	2.24	2.08[b]	2.23(2.24)	2.24[ab]	2.43(2.42)	2.43[ab]
	D [cm^{-1}]	--	--	-7.4(-7.4)	-7.77[ab]	109.0(115.2)	108.0[ab]
	E/*D*	--	--	0.029(0.040)	0.02[ab]	0.050(0.067)	0.043[ab]

[a]Only the PBE0 geometry was employed.
[b]Using the DLPNO-NEVPT2 formalism.

Table S7: Best computational estimates for ***g*** and ***D*** tensors, obtained at the DLPNO-NEVPT2 level for the medium-size cluster models optimized with PBE0.

Property	**Cu**	**Ni**	**Co**
$g_{\perp}$[a]	2.13	2.27	1.88
$g_{\parallel}$[b]	2.06	2.22	2.71
g_{iso}	2.08	2.24	2.43
D [cm^{-1}]	--	-7.8	108.0
E [cm^{-1}]	--	0.2	4.6
E/D	--	0.021	0.043

[a]In the direction perpendicular to the LDH layers.
[b]In the plane of the LDH layers.

S4: Computational *J* Error Margins

To gain a rough estimate of methodological error margins for the exchange coupling computations, different sets of in-chain exchange coupling, *J*, calculations were performed (Table S5). These include the (1) standard PBE0 functional for cluster models geometry-optimized with PBE, (2) PBE0 functional for cluster models geometry-optimized with PBE0, and (3) using the PBE0-40 functional (instead of standard PBE0) for the PBE0-optimized cluster geometry. Moreover, for each set of calculations, either the SVP basis set or locally dense QZVPP/SVP basis were used, *i.e.*, QZVPP on the MO_6-cordination sphere and SVP otherwise. For the $CoAl_4$-LDH clusters, the QZVPP/SVP basis set proved, in some cases occurring both in the models for *J* and *j*, extremely challenging in terms of computation time and/or attainable numerical precision. Consequently, certain results are only reported with the SVP basis for the $CoAl_4$-LDH system.

The cluster models run with locally dense QZVPP/SVP basis, as opposed to using the small SVP basis for the entire system, optimized using the hybrid PBE0 functional and dispersion corrections, are expected to give the most accurate results. Typically, hybrid functionals such as PBE0 perform better for magnetic properties than pure DFT functionals such as PBE, and a coarse estimate

of the error may be obtained by varying the exact-exchange admixture in the functional, *e.g.*, by using 40% exchange as in PBE0-40 presently.[32] The broken-symmetry (BS) results, obtained by the PBE0 or PBE0-40 functional on the large in-chain clusters, give J of 0.65 and 0.55 cm^{-1} for the $CuAl_4$-LDH, 0.27 and 0.14 cm^{-1} for $NiAl_4$-LDH, and 0.06 and 0.03 cm^{-1} for $CoAl_4$-LDH (SVP data used for $CoAl_4$-LDH), with PBE0 and PBE0-40, respectively. Similar results are obtained in the flip-spin formalism (FS), where J of 0.72 and 0.42 cm^{-1} are obtained for $CuAl_4$-LDH, 0.17 and 0.19 cm^{-1} for $NiAl_4$-LDH, and 0.10 and 0.08 cm^{-1} for $CoAl_4$-LDH (with QZVPP/SVP), with the PBE0 and PBE0-40 functionals, respectively. We assign our error margins to the PBE0 – PBE0-40 difference in this work.

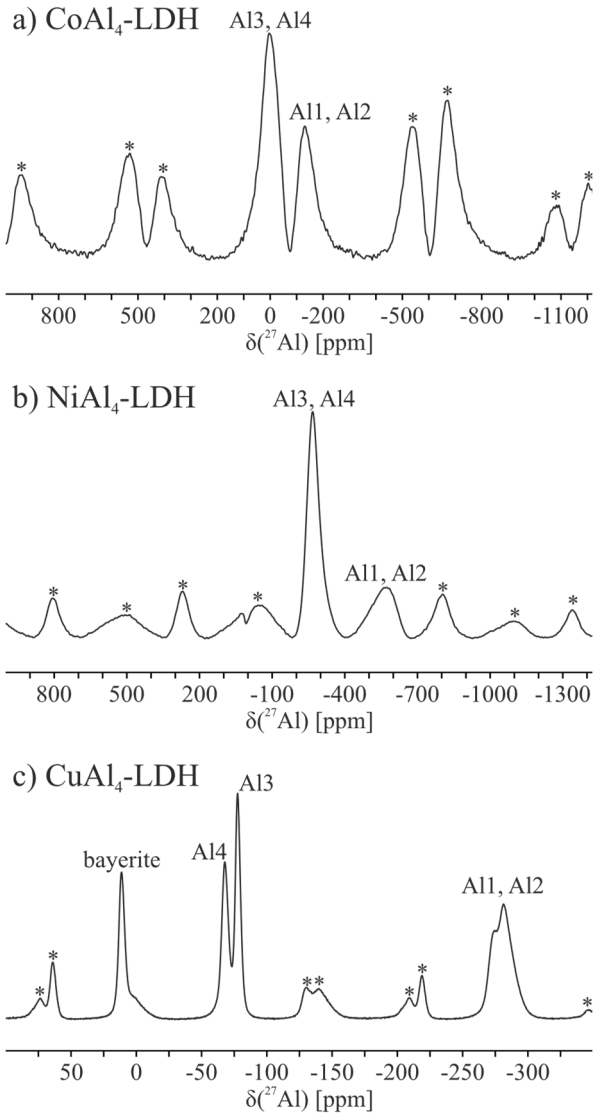

Fig. S10: The isotropic region of the single-pulse ^{27}Al MAS NMR spectra of **a)** $CoAl_4$-LDH (70 kHz spinning speed, 11.7 T), **b)** $NiAl_4$-LDH (70 kHz spinning speed, 11.7 T), and **c)** $CuAl_4$-LDH, which has ca 10 wt% bayerite (31 kHz spinning speed, 14.1 T). Spinning sidebands (ssb) are marked by an asterisk. See Ref.[33] for further information

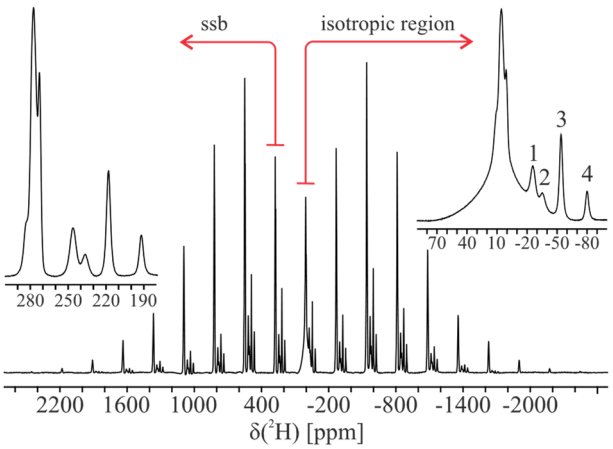

Fig. S11: ^{2}H MAS NMR spectrum of D-CuAl$_4$-LDH (20-25 kHz spinning speeds, 14.1 T field). The insets show (right) the four distinct hyperfine $\delta_{iso}(^{2}H)$ regions indicated by 1, 2, 3, and 4 as well as the broad resonance from physiosorbed water around 0 ppm with the diamagnetic Al-OH groups superimposed and (left) a zoom of the first spinning sideband on the left from these four regions.

References

1. R. Boča, *Coordination Chemistry Reviews*, 2004, **248**, 757-815.
2. S. S. C. Pushparaj, N. D. Jensen, C. Forano, G. J. Rees, V. Prevot, J. V. Hanna, D. B. Ravnsbæk, M. Bjerring and U. G. Nielsen, *Inorganic Chemistry*, 2016, **55**, 9306–9315.
3. N. D. Jensen, N. T. Duong, R. Bolanz, Y. Nishiyama, C. A. Rasmussen, J. Gottlicher, R. Steininger, V. Prevot and U. G. Nielsen, *Inorganic Chemistry*, 2019, **58**, 6114-6122.
4. J. I. Facio, D. Betancourth, N. R. Cejas Bolecek, G. A. Jorge, P. Pedrazzini, V. F. Correa, P. S. Cornaglia, V. Vildosola and D. J. García, *Journal of Magnetism and Magnetic Materials*, 2016, **407**, 406-411.
5. J. W. Kim, Y. S. Oh, K. S. Suh, Y. D. Park and K. H. Kim, *Thermochimica Acta*, 2007, **455**, 2-6.
6. L. Yang, M. Jeong, P. Babkevich, V. M. Katukuri, B. Náfrádi, N. E. Shaik, A. Magrez, H. Berger, J. Schefer, E. Ressouche, M. Kriener, I. Živković, O. V. Yazyev, L. Forró and H. M. Rønnow, *Physical Review B*, 2017, **96**, 024445.
7. P. Fischer, G. Frey, M. Koch, M. Könnecke, V. Pomjakushin, J. Schefer, R. Thut, N. Schlumpf, R. Bürge, U. Greuter, S. Bondt and E. Berruyer, *Physica B: Condensed Matter*, 2000, **276-278**, 146-147.
8. S. Janßen, J. Mesot, L. Holitzner, A. Furrer and R. Hempelmann, *Physica B: Condensed Matter*, 1997, **234-236**, 1174-1176.
9. W. Marshall and S. W. Lovesey, *Theory of Thermal Neutron Scattering*, Oxford University Press1971.
10. O. Arnold, J. C. Bilheux, J. M. Borreguero, A. Buts, S. I. Campbell, L. Chapon, M. Doucet, N. Draper, R. Ferraz Leal, M. A. Gigg, V. E. Lynch, A. Markvardsen, D. J. Mikkelson, R. L. Mikkelson, R. Miller, K. Palmen, P. Parker, G. Passos, T. G. Perring, P. F. Peterson, S. Ren, M. A. Reuter, A. T. Savici, J. W. Taylor, R. J. Taylor, R. Tolchenov, W. Zhou and J. Zikovsky, *Nuclear Instruments and Methods in Physics Research Section A: Accelerators, Spectrometers, Detectors and Associated Equipment*, 2014, **764**, 156-166.
11. P. J. Brown, in *Neutron Data Booklet*, eds. A.-J. Dianoux and G. Lander, OCP Science Imprint2002.
12. F. Neese and F. Wennmohs, *ORCA Manual version 4.2.1*2019.
13. A. P. Ginsberg, *Journal of the American Chemical Society*, 1980, **102**, 111-117.
14. L. Noodleman, *The Journal of Chemical Physics*, 1981, **74**, 5737-5743.
15. A. Bencini and D. Gatteschi, *Journal of the American Chemical Society*, 1986, **108**, 5763-5771.
16. K. Yamaguchi, Y. Takahara and T. Fueno, in *Applied Quantum Chemistry*, ed. V. H. Smith, Wiley, Reidel, Dordrecht1986, p. 155.
17. T. Soda, Y. Kitagawa, T. Onishi, Y. Takano, Y. Shigeta, H. Nagao, Y. Yoshioka and K. Yamaguchi, *Chemical Physics Letters*, 2000, **319**, 223-230.
18. E. Sokolova, F. C. Hawthorne, Y. A. Uvarova, A. A. Agakhanov, L. A. Pautov and V. V. Karpenko, *The Canadian Mineralogist*, 2005, **43**, 1511-1519.
19. K. Momma and F. Izumi, *Journal of Applied Crystallography*, 2011, **44**, 1272-1276.
20. J. Sauer, *Chemical Reviews*, 1989, **89**, 199-255.
21. Turbomole, version 7.2., 2017, pp. a development of University of Karlsruhe and Forschungszentrum Karlsruhe GmbH, 1989-2007, TURBOMOLE GmbH, since 2007.
22. J. P. Perdew, K. Burke and M. Ernzerhof, *Physical Review Letters*, 1996, **77**, 3865-3868.

23. J. P. Perdew, K. Burke and M. Ernzerhof, *Physical Review Letters*, 1997, **78**, 1396-1396.
24. C. Adamo and V. Barone, *The Journal of Chemical Physics*, 1999, **110**, 6158-6170.
25. S. Grimme, J. Antony, S. Ehrlich and H. Krieg, *The Journal of Chemical Physics*, 2010, **132**, 154104.
26. S. Grimme, S. Ehrlich and L. Goerigk, *Journal of Computational Chemistry*, 2011, **32**, 1456-1465.
27. M. Dolg, U. Wedig, H. Stoll and H. Preuß, *The Journal of Chemical Physics*, 1987, **86**, 866-872.
28. F. Weigend and R. Ahlrichs, *Physical Chemistry Chemical Physics*, 2005, **7**, 3297-3305.
29. D. Ganyushin and F. Neese, *The Journal of Chemical Physics*, 2006, **125**, 024103.
30. D. Ganyushin and F. Neese, *The Journal of Chemical Physics*, 2013, **138**, 104113.
31. Y. Guo, K. Sivalingam, E. F. Valeev and F. Neese, *The Journal of Chemical Physics*, 2016, **144**, 094111.
32. J. Vaara, *Physical Chemistry Chemical Physics*, 2007, **9**, 5399-5418.
33. A. B. A. Andersen, C. Henriksen, Q. Wang, D. B. Ravnsbæk, L. P. Hansen and U. G. Nielsen, *Inorganic Chemistry*, 2021, **60**, 16700-16712.